

THE LARGE SCALE BIAS OF DARK MATTER HALOS: NUMERICAL CALIBRATION AND MODEL TESTS

JEREMY L. TINKER¹, BRANT E. ROBERTSON^{2,10}, ANDREY V. KRAVTSOV^{3,4,5}, ANATOLY KLYPIN⁶,
MICHAEL S. WARREN⁷, GUSTAVO YEPES⁸, STEFAN GOTTLÖBER⁹

Draft version November 26, 2024

ABSTRACT

We measure the clustering of dark matter halos in a large set of collisionless cosmological simulations of the flat Λ CDM cosmology. Halos are identified using the spherical overdensity algorithm, which finds the mass around isolated peaks in the density field such that the mean density is Δ times the background. We calibrate fitting functions for the large scale bias that are adaptable to any value of Δ we examine. We find a $\sim 6\%$ scatter about our best fit bias relation. Our fitting functions couple to the halo mass functions of Tinker et. al. (2008) such that bias of all dark matter is normalized to unity. We demonstrate that the bias of massive, rare halos is higher than that predicted in the modified ellipsoidal collapse model of Sheth, Mo, & Tormen (2001), and approaches the predictions of the spherical collapse model for the rarest halos. Halo bias results based on friends-of-friends halos identified with linking length 0.2 are systematically lower than for halos with the canonical $\Delta = 200$ overdensity by $\sim 10\%$. In contrast to our previous results on the mass function, we find that the universal bias function evolves very weakly with redshift, if at all. We use our numerical results, both for the mass function and the bias relation, to test the peak-background split model for halo bias. We find that the peak-background split achieves a reasonable agreement with the numerical results, but $\sim 20\%$ residuals remain, both at high and low masses.

Subject headings: cosmology:theory — methods:numerical — large scale structure of the universe

1. INTRODUCTION

Dark matter halos are biased tracers of the underlying dark matter distribution. Massive halos form from high- σ fluctuations in the primordial density field, inducing a correlation between halo mass and clustering amplitude that is steepest for cluster-sized objects (Kaiser 1984). Low-mass halos are preferentially found in regions of the universe with below average density, thus these objects are anti-biased with respect to the dark matter. The clustering of galaxies is now understood through the bias of the halos in which they form (e.g., Zehavi et al. 2005). Many methods that utilize galaxy clustering to constrain cosmology require precise knowledge of halo clustering (e.g., van den Bosch et al. 2003; Tinker et al. 2005; Abazajian et al. 2005; Zheng & Weinberg 2007; Yoo et al. 2009). Cosmological parameters can also be obtained through the abundance of high-mass halos identified as galaxy clusters. The bias of clusters contains complementary information to their abundance. Indeed, “self-calibration” of cluster surveys is not possible without the additional information present in clustering data (Lima & Hu 2004, 2005; Majumdar & Mohr 2004; Oguri 2009). The purpose of this paper is to calibrate a precise, flexible halo bias function from numerical simulations that is accurate for dwarf

galaxies through galaxy cluster masses.

In Tinker et al. (2008) (hereafter T08), we presented a recalibration of the halo mass function based on a large series of collisionless N-body simulations. Our results utilized the spherical overdensity (SO) algorithm for identifying dark matter halos within simulations (e.g., Lacey & Cole 1994). In this approach, halos are identified as isolated density peaks, and the mass of a halo is determined by the overdensity Δ , defined here as the mean interior density relative to the background. Simulations of cluster formation show that the SO-defined halo mass should correlate tightly with cluster observables, which are usually defined within a spherical aperture (e.g., Bialek et al. 2001; da Silva et al. 2004; Nagai 2006; Kravtsov et al. 2006). This expectation is borne out for observables such as gas mass, core-excised luminosity, integrated SZ flux or its X-ray analog, Y_X (e.g., Mohr et al. 1999; Vikhlinin et al. 2006; Zhang et al. 2008; Vikhlinin et al. 2009; Arnaud et al. 2007, 2009; Sun et al. 2009). Tight correlations between spherical overdensity mass and observables are crucial for a robust interpretation of the observed cluster counts and clustering in deriving cosmological constraints. The scatter of mass-observable relations may depend on the value of Δ . In addition, particular observations may only extend out to a limited radius corresponding to Δ considerably higher than the often used virial value of $\Delta \approx 200$. Thus, we seek to calibrate a fitting function that can be adapted to any value of Δ .

Hu & Kravtsov (2003) and Manera et al. (2009) compared existing halo bias models to SO N-body results at the cluster mass scale. But previous studies to calibrate halo bias on numerical simulations have focused exclusively on the friends-of-friends (FOF) halo finding algorithm (Jing 1998, 1999; Sheth & Tormen 1999; Sheth et al. 2001; Seljak & Warren 2004; Tinker et al. 2005; Pillepich et al. 2008; Reed et al. 2008). The FOF algorithm is a percolation scheme that makes no assumptions about halo geometry, but may spuriously group distinct halos together into the same object, con-

¹ Berkeley Center for Cosmological Physics, University of California, Berkeley

² Astronomy Department, California Institute of Technology, MC 249-17, 1200 East California Boulevard, Pasadena, CA 91125

³ Kavli Institute for Cosmological Physics, The University of Chicago, 5640 S. Ellis Ave., Chicago, IL 60637, USA

⁴ Department of Astronomy & Astrophysics, The University of Chicago, 5640 S. Ellis Ave., Chicago, IL 60637, USA

⁵ Enrico Fermi Institute, The University of Chicago, 5640 S. Ellis Ave., Chicago, IL 60637, USA

⁶ Department of Astronomy, New Mexico State University

⁷ Theoretical Astrophysics, Los Alamos National Labs

⁸ Grupo de Astrofísica, Universidad Autónoma de Madrid

⁹ Astrophysikalisches Institut Potsdam, Potsdam, Germany

¹⁰ Hubble Fellow

fusing the comparison between cluster observables theoretical results (White 2001; Tinker et al. 2008; Lukić et al. 2009). Additionally, previous calibrations focus on only one value of the FOF linking length, $l = 0.2$, and thus are not applicable to many mass observables. Galaxy cluster studies and theoretical halo models benefit from a self-consistently defined set of coupled mass and bias functions.

The bias of halos is determined by the relative abundance of halos in different large-scale environments. Thus, theoretical models for halo bias have been derived from the mass function using the peak-background split (Bardeen et al. 1986; Cole & Kaiser 1989; Mo & White 1996; Sheth & Tormen 1999; Sheth et al. 2001). These models produce results that are reasonably accurate but fail to reproduce in detail the bias of halos found in numerical simulations (Jing 1998; Seljak & Warren 2004; Tinker et al. 2005; Gao et al. 2005; Pillepich et al. 2008). Manera et al. (2009) and Manera & Gaztanaga (2009) demonstrate that using the peak background split to calculate the bias of massive halos from their mass function does not accurately match the clustering as measured from their spatial distribution. In addition to calibrating the functional form of the bias, we test the peak background split.

In §2 we summarize our list of simulations and the numerical techniques for calculating bias. In §3 we present our fitting formulae for large scale bias, comparing to previous works and exploring any redshift evolution. In §4 we use our results to test the peak-background split. In §5 we summarize our results.

2. SIMULATIONS AND METHODS

Our simulation set spans a wide range in volume and mass resolution in order to produce results than span nearly six decades in mass, from $M \sim 10^{10} h^{-1} M_{\odot}$ halos to massive clusters. The set contains 15 distinct simulations that span local variations of the concordance Λ CDM cosmology consistent with results from CMB anisotropies (Spergel et al. 2003; Dunkley et al. 2009). Three numerical codes are represented in our set; the adaptive refinement technique (ART; Kravtsov et al. 1997; Gottlöber & Klypin 2008), the hashed oct-tree code (HOT; Warren et al. 2006), and the hybrid tree-particle mesh code GADGET2 (Springel 2005). Table 1 lists details of each simulation, including cosmological parameters, force resolution, volume, and mass resolution. Further details about the simulation set can be found in T08. For one simulation, L1280, there are 49 independent realizations. The L1280 simulations were utilized in the studies on the halo mass function and bias relation of massive halos in Crocce et al. (2006) and Manera et al. (2009), as well as in the analysis in T08. The dark matter outputs of these simulations were kindly supplied by R. Scoccimarro.

Crocce et al. (2006) point out that improper initial conditions can result in errors in the resulting halo mass function and, to a lesser extent, bias function for massive halos. These errors are a product of starting the simulation at too low a redshift while using first-order techniques for the initial particle displacements and velocities. The L1280 simulations utilize second-order perturbation theory to ameliorate these effects. In T08 we performed multiple re-simulations of L1000W with initial conditions set using the Zel’dovich approximation at different redshifts. We found significant differences between the mass functions measured in the L1000W run with Zel’dovich initial conditions set at $z=30$ and the mass function measured in the L1280 run. However, using Zel’dovich ini-

tial conditions at $z=60$ for L1000W produces a mass function negligibly different from the L1280 calculations.

Halos are identified in each simulation using the spherical overdensity (SO) technique outlined in T08. In brief, the code identifies density peaks in the dark matter and grows spheres around them until the mean interior density is some set multiple, Δ , of the background density. Thus the mass and radius of a halo are related by

$$M_{\Delta} = \frac{4}{3}\pi R_{\Delta} \bar{\rho}_m(z) \Delta, \quad (1)$$

where $\bar{\rho}_m(z)$ is the mean density of the universe at redshift z . In our implementation of the SO algorithm, the spheres that contain halos are allowed to overlap; so long as the center of one halo is not contained within R_{Δ} of another halo, the two halos are considered distinct. Owing to small overlaps in the exteriors of halos, a small fraction of the total mass in halos ($\sim 0.7\%$) is assigned to multiple halos and double counted. The SO method of identifying halos makes the halo mass sensitive to the force resolution of the simulation; if the density profile of a halo is not properly resolved, the enclosed mass at a given radius will be smaller. Column 10 in Table 1 lists the maximum value of Δ for which reliable results could be obtained for each simulation. Owing to the low spatial resolution of the L1280 simulations, our analysis only utilizes these simulations for $\Delta = 200$. For all simulations, only halos with more than 400 particles are used. This ensures that all halos are robustly identified and the halo profiles are well sampled.

We define the bias of dark matter halos as the ratio of the halo power spectrum to the linear dark matter power spectrum,

$$b^2(k) = \frac{P_h(k)}{P_{\text{lin}}(k)}. \quad (2)$$

We calculate the power spectrum of each simulation as follows. The halos of each simulation are binned in a 200^3 density mesh using the cloud-in-cell technique, and the power spectrum is computed through Fourier transformation. All power spectra are shot-noise subtracted. Aliasing due to the cloud-in-cell grid is removed through the deconvolution technique outlined in Jing (2005). Although halo bias is scale-dependent in the quasi-linear and non-linear regime, here we focus on the large scale bias, where b is independent of k . We calculate b^2 as the average over the 10 largest wavelength modes in the simulation. For simulations with $L_{\text{box}} < 200 h^{-1} \text{Mpc}$, non-linearity has set in at $k \gtrsim 10 \times 2\pi/L_{\text{box}}$. For these simulations, we truncate our average to the largest 5 modes. For the $z = 2.5$ outputs of two simulations, L120W and L120, the power spectra do not converge to a robust asymptotic value within this k -range, thus we exclude these outputs from the analysis. For each simulation, we calculate $P_h(k)$ for 8 jackknife subsamples of the simulation, removing density fluctuations from one octant of the box in each subsample. We use the jackknife subsamples to estimate the error on b .

We also check these results against bias as defined by the halo-mass cross-power spectrum $b_{hm} = P_{hm}/P_{\text{lin}}$. This measure does not require a shot noise correction, and it yields better statistics when the halos become vary sparse.

We parameterize our results in terms of ‘peak height’ in the linear density field, $\nu = \delta_c/\sigma(M)$, where δ_c is the critical density for collapse and σ is the linear matter variance on the Lagrangian scale of the halo, ie, $R = (3M/4\pi\bar{\rho}_m)^{1/3}$, defined as

TABLE 1
PROPERTIES OF THE SIMULATION SET

$L_{\text{box}} h^{-1} \text{Mpc}$	Name	$\epsilon h^{-1} \text{kpc}$	N_p	$m_p h^{-1} M_{\odot}$	$(\Omega_m, \Omega_b, \sigma_8, h, n)$	Code	z_i	z_{out}	Δ_{max}
768	H768	25	1024^3	3.51×10^{10}	(0.3, 0.04, 0.9, 0.7, 1)	HOT	40	0	800
384	H384	14	1024^3	4.39×10^9	(0.3, 0.04, 0.9, 0.7, 1)	HOT	48	0	3200
271	H271	10	1024^3	1.54×10^9	(0.3, 0.04, 0.9, 0.7, 1)	HOT	51	0	3200
192	H192	4.9	1024^3	5.89×10^8	(0.3, 0.04, 0.9, 0.7, 1)	HOT	54	0	3200
96	H96	1.4	1024^3	6.86×10^7	(0.3, 0.04, 0.9, 0.7, 1)	HOT	65	0	3200
1280	L1280	120	640^3	5.99×10^{11}	(0.27, 0.04, 0.9, 0.7, 1)	GADGET2	49	0, 0.5, 1.0	600
500	L500	15	$1024^3 \times 2$	8.24×10^9	(0.3, 0.045, 0.9, 0.7, 1)	GADGET2	40	0, 0.5, 1.25, 2.5	3200
250	L250	7.6	512^3	9.69×10^9	(0.3, 0.04, 0.9, 0.7, 1)	ART	49	0, 0.5, 1.25, 2.5	3200
120	L120	1.8	512^3	1.07×10^9	(0.3, 0.04, 0.9, 0.7, 1)	ART	49	0, 0.5, 1.25, 2.5	3200
80	L80	1.2	512^3	3.18×10^8	(0.3, 0.04, 0.9, 0.7, 1)	ART	49	0, 0.5, 1.25, 2.5	3200
1000	L1000W	30	1024^3	6.98×10^{10}	(0.27, 0.044, 0.79, 0.7, 0.95)	ART	60	0, 0.5, 1.0, 1.25	3200
384	H384W	14	1024^3	3.80×10^9	(0.26, 0.044, 0.75, 0.71, 0.94)	HOT	35	0	3200
384	H384 Ω_m	14	1024^3	2.92×10^9	(0.2, 0.04, 0.9, 0.7, 1)	HOT	42	0	3200
120	L120W	0.9	1024^3	1.21×10^8	(0.27, 0.044, 0.79, 0.7, 0.95)	ART	100	1.25, 2.5	3200
80	L80W	1.2	512^3	2.44×10^8	(0.23, 0.04, 0.75, 0.73, 0.95)	ART	49	0, 0.5, 1.25, 2.5	3200

NOTE. — The top set of 5 simulations are from the Warren et al. (2006) study. The second list of 5 simulations are of the same WMAP1 cosmology, but with different numerical codes. The third list of 5 simulations are of alternate cosmologies, focusing on the WMAP3 parameter set. The HOT code employs Plummer softening, while GADGET employs spline softening. The values of ϵ listed for the GADGET simulations are the equivalent Plummer softening; when calculating the spline softening kernel, GADGET uses a value of 1.4ϵ . The force resolution of the ART code is based on the size of the grid cell at the highest level of refinement. Δ_{max} is the highest overdensity for which halo masses can be reliably measured.

$$\sigma^2(R) = \frac{1}{2\pi^2} \int P(k, z) \hat{W}^2(k, R) k^2 dk, \quad (3)$$

where $P(k, z)$ is the linear power spectrum at redshift z and \hat{W} is the Fourier transform of the top-hat window function of radius R . In all calculations we use $\delta_c = 1.686$. For reference, ν of 0.75, 1, 2, and 3 ($\log \nu = [-0.12, 0.0, 0.30, 0.48]^{11}$) corresponds to M of 2.9×10^{11} , 2.8×10^{12} , 1.2×10^{14} , and $7.0 \times 10^{14} h^{-1} M_{\odot}$, respectively, for the L1000W cosmology at $z = 0$.

3. RESULTS

3.1. Models and Measurements at $\Delta = 200$

Figure 1 shows bias as a function of ν for all simulations in Table 1. In this figure, halos are defined with $\Delta = 200$. In the spherical collapse model, $\Delta \approx 200$ defines a radius separating the virialized region and the region of continuing infall in an $\Omega_m = 1$ universe (Lacey & Cole 1994; Eke et al. 1998). This overdensity is also close to the overdensity of halos identified with the friends-of-friends (FOF) algorithm with the typical linking parameter of 0.2 (Davis et al. 1985). Thus analytic models are typically compared to numerical results using either $\Delta = 200$ or FOF(0.2). In Figure 1, we compare our $\Delta = 200$ results to two current models for halo bias from the literature.

First, we compare these results to predictions based on the spherical collapse model (SC) for the formation of dark matter halos. In SC, halos collapse when the linear overdensity associated with a peak in the density field crosses a critical barrier δ_c independent of halo mass. Press & Schechter (1974) used this model to derive an expression for the mass function of dark matter halos. Using the peak-background split, which we will describe in more detail in section §4, Cole & Kaiser (1989) and Mo & White (1996) derived a bias relation of the form

$$b(\nu) = 1 + \frac{\nu^2 - 1}{\delta_c}. \quad (4)$$

However, the Press-Schechter mass function fails to reproduce the dark matter halo mass function found in simulations (see, e.g., Gross et al. 1998; Lee & Shandarin 1999; Sheth & Tormen 1999; Jenkins et al. 2001; Robertson et al. 2009). Thus it is not surprising that the bias function in equation (4) also does not compare well to simulations (see, e.g., Jing 1998, 1999; Sheth & Tormen 1999). In Figure 1, the SC model overpredicts the bias in the range $1 \lesssim \nu \lesssim 3$, while underpredicting slightly the bias for the lowest mass halos in our simulations.

Sheth & Tormen (1999) (hereafter ST) generalized the expression for the Press-Schechter mass function and calibrated the free parameters using numerical simulations. Sheth et al. (2001) (hereafter SMT) later refined this calculation, incorporating a “moving” barrier for the collapse criterion of halos in which the critical density varies with the peak height as motivated by the more physically realistic ellipsoidal collapse model. Using the peak-background split once again, SMT derived an improved expression for bias of the form

$$b(\nu) = 1 + \frac{1}{\sqrt{a}\delta_c} \left[\sqrt{a}(a\nu^2) + \sqrt{ab}(a\nu^2)^{1-c} - \frac{(a\nu^2)^c}{(a\nu^2)^c + b(1-c)(1-c/2)} \right], \quad (5)$$

where $a = 0.707$, $b = 0.5$, and $c = 0.6$. These parameters describe the shape of the moving barrier. In Figure 1, the SMT bias equation underpredicts the clustering of high-peak halos while overpredicting the asymptotic bias of low-mass objects. The SMT function is calibrated using friends-of-friends (FOF) halos, thus the choice of Δ with which to compare is somewhat arbitrary, but it can be seen that the SMT function and our results will not agree at any overdensity: SMT bias at low ν is too high, and is too low at high ν . When increasing (decreasing) Δ , the bias at all ν can only increase (decrease).

¹¹ Throughout this paper, log indicates base-10 logarithm.

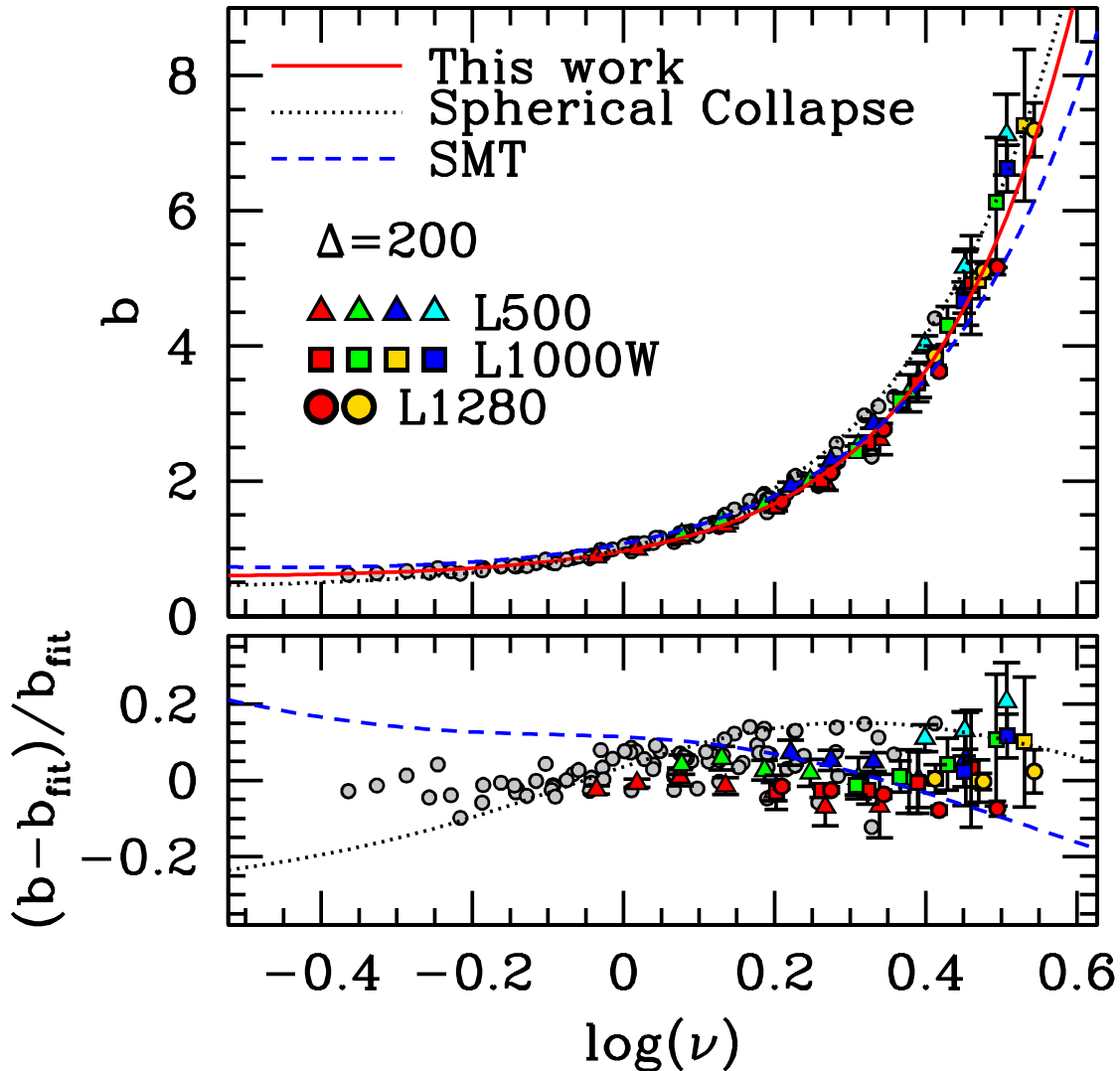


FIG. 1.— *Upper Panel*: Large-scale bias as determined by the ratio $(P_h/P_{\text{lin}})^{1/2}$ for $\Delta = 200$. Results from the smaller boxes are represented by the gray circles. For these simulations, only measurements with less than 10% error are shown to avoid crowding. The larger-volume simulations are represented by the colored symbols. Each point type indicates a different simulation. The different colors, from left to right, go in order of increasing redshift from $z = 0$ to $z = 2.5$ (see Table 1 for the redshift outputs of each simulation). Like colors between simulations imply the same redshift. For these large-volume simulations, measurements with less than 25% errors are shown. *Lower Panel*: Fractional differences of the N-body results with the the fitting function shown in the upper panel.

The bias formulae of ST and SMT have been shown before to be inaccurate at low masses (Seljak & Warren 2004; Tinker et al. 2005; Gao et al. 2005; Pillepich et al. 2008). Updated fitting functions have sometimes used the functional form of ST (Mandelbaum et al. 2005) or SMT (Tinker et al. 2005) with new parameters chosen to match numerical data, while others have proposed entirely new functional forms (e.g., Seljak & Warren 2004; Pillepich et al. 2008). Our tests show that the SMT function does not yield optimal χ^2 values when comparing to our numerical results. We therefore introduce a similar but more flexible fitting function of the form

$$b(\nu) = 1 - A \frac{\nu^a}{\nu^a + \delta_c^a} + B\nu^b + C\nu^c. \quad (6)$$

Equation (6) scales as a power-law at the highest masses, flattens out at low masses and asymptotes to $b = 1$ at $\nu = 0$, pro-

vided $a > 0$.

A convenient property of the SC, ST, and SMT functions is that they are normalized such that the mean bias of halos is unity. Thus, if one adopts the halo model ansatz that all mass is contained within halos, dark matter is not biased against itself. Numerically calibrated bias functions in the literature do not obey this constraint (Jing 1998, 1999; Tinker et al. 2005; Seljak & Warren 2004; Pillepich et al. 2008). When fitting for the parameters of equation (6), we enforce this constraint by requiring that our bias function obey the relation

$$\int b(\nu)f(\nu)d\nu = 1, \quad (7)$$

where $f(\nu)$ is the halo mass function, once again expressed in terms of the scaling variable ν . At each Δ , we use the halo mass functions listed in Appendix C of T08, which are nor-

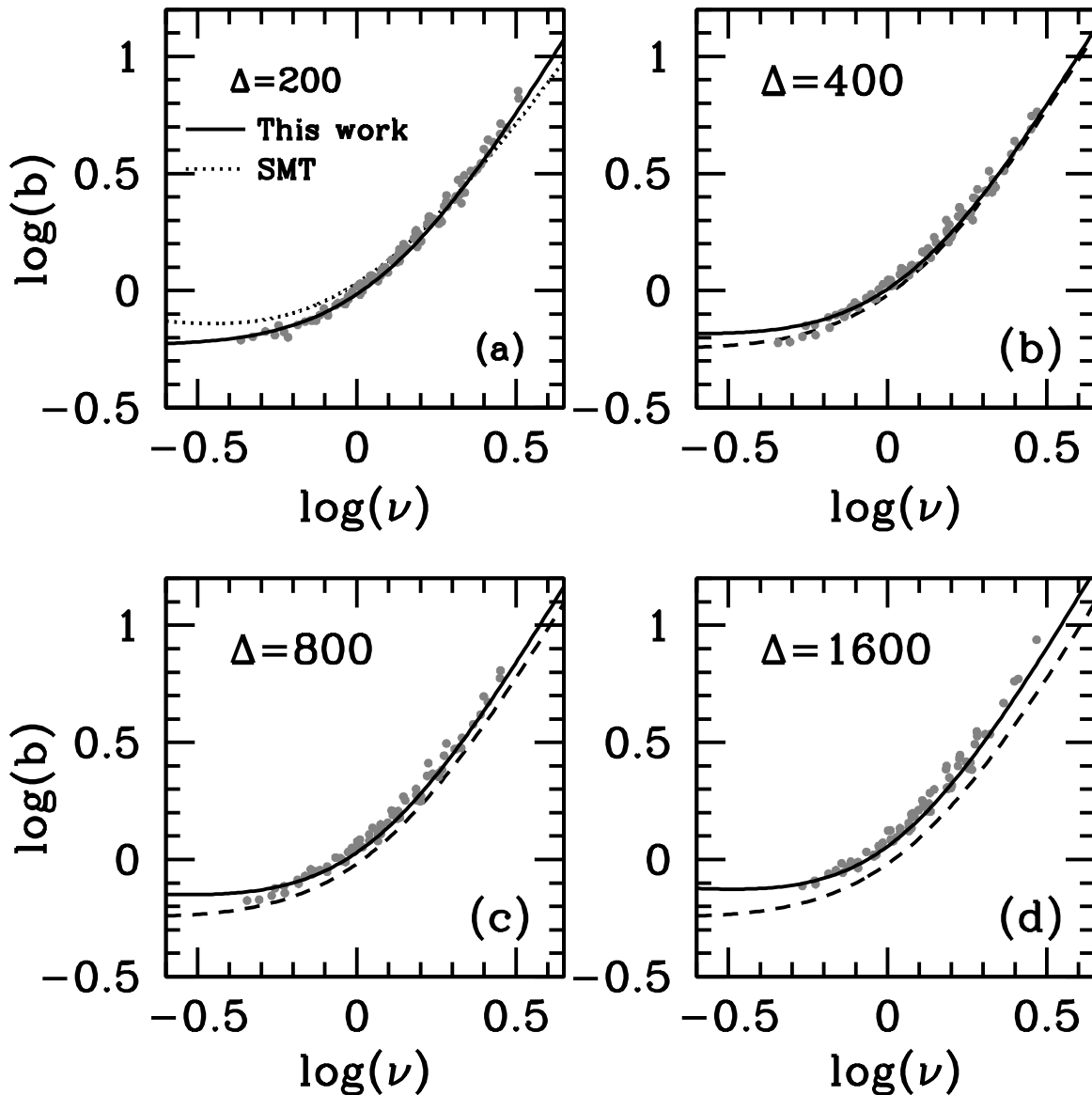


FIG. 2.— Large-scale bias as determined by the ratio $(P_h/P_{\text{lin}})^{1/2}$ for four values of Δ . The solid line in each panel represents equation (6) with the Δ -dependent parameters listed in Table 2. The dotted curve in panel (a) is the bias formula of SMT. The dashed curve in panels (c)-(d) is the $\Delta = 200$ results (i.e., the solid curve in panel a).

malized such that the mean density of the universe is obtained when integrating over all halo masses at $z=0$ ¹².

In T08, we found that the mass function is universal at $z=0$ over the range of cosmologies explored. However, the mass function at higher redshifts deviates systematically from the $z=0$ results. In Figure 1, we have included the results from *all* redshifts. Although the evolution of $f(\sigma)$ from $z=0$ to $z=1$ is clear in the T08 results, the bias of these halos does not show significant evolution with redshift. To obtain the parameters of equation (6), we minimize the χ^2 using the jackknife errors described in the previous section. The best-fit parameters for the $\Delta = 200$ data, listed in Table 2, yield a χ^2 per degree of freedom (hereafter χ_ν^2) of 1.9 when incorporating all data from all redshifts. This high value of χ_ν^2 is driven

by the small error bars on the L1280 results at $z=0$. With 49 realizations, the error bars are $\sim 1\%$ at the low-particle limit, thus the few percent offset between the L1280 results and those of the remaining simulations yields a high χ_ν^2 . Removing the L1280 results (without refitting) yields $\chi_\nu^2 = 1.01$. The low spatial resolution of the L1280 simulations is a possible source of error in the bias results. Refitting with only the $z=0$ results does not change the values of the best-fit parameters or change χ_ν^2 . This implies that the evolution of bias with redshift is extremely weak between $0 \leq z \leq 2.5$, if it evolves at all. Simulation to simulation, the situation is not definitive. The L500 simulations shows an increased amplitude in the bias of $\sim 5\%$ between $z=0$ and $z=1.25$, but the L1000W simulation is consistent at all redshifts. Regardless, any evolution in the bias function at fixed ν is significantly smaller than the evolution in the mass function.

¹² The normalized mass functions in T08 are expressed in terms of $1/\sigma$ rather than ν . For convenience we rewrite this function in terms of ν in Equation (8) and give new mass function parameter values in Table 4.

3.2. Large-Scale Bias as a Function of Δ

TABLE 2
PARAMETERS OF BIAS EQUATION
(6) AS A FUNCTION OF Δ

parameter	$f(\Delta)$
A	$1.0+0.24y\exp[-(4/y)^4]$
a	$0.44y-0.88$
B	0.183
b	1.5
C	$0.019+0.107y+0.19\exp[-(4/y)^4]$
c	2.4

NOTE. — Note: $y \equiv \log_{10} \Delta$.

TABLE 3
 χ^2_ν VALUES OF THE $b(\nu)$ FITS

Δ	χ^2_ν
200	1.01/1.94
300	1.33
400	1.08
600	1.34
800	1.19
1200	1.22
1600	1.14
2400	1.06
3200	1.08

NOTE. — For $\Delta = 200$, the second value of χ^2_ν includes the L1280 simulations.

The best-fit parameters of equation (6) scale smoothly with Δ , allowing us to obtain fitting functions for these parameters as a function of $\log \Delta$. The functions that yield the parameters of equation (6) for $200 \leq \Delta \leq 3200$ are listed in Table 2. Using these functions, the integral constraint in equation (7) is satisfied to better than 1% for every value of Δ considered. If required, higher precision can be obtained if 5 of the 6 parameters are taken from Table 2 and the last is solved for numerically.

A comparison between our numerical results and fitting functions for four values of Δ are shown in Figure 2. To avoid crowding and scatter, in each panel we only plot data points with fractional errors less than 10%. Figures 2b-2d compare the results for $\Delta = 400, 800,$ and 1600 to the $\Delta = 200$ fitting function (shown against the $\Delta = 200$ data from 2a). As Δ increases, bias increases at all mass scales. At high masses this is expected; as Δ increases, a fixed set of halos will have lower masses but the same clustering properties, essentially shifting them along the ν -axis. At low masses, the amplitude of the bias curve also monotonically increases with Δ , owing to the substructure within high mass halos that become distinct objects as R_Δ decreases. Because these new low mass halos are in the vicinity of high mass objects, they have significant clustering.¹³

¹³ In principle, this makes our results sensitive to the spatial resolution of our simulations beyond simply resolving the halo density profiles properly. If subhalos are not resolved in some subset of our simulations, the change in bias for low ν halos will be underpredicted. Our criterion for including simulations in our analysis is that halo density profiles are properly resolved, not that substructure is properly resolved. However, the fact that bias monotonically increases with Δ at low ν is indicative that we are including these “revealed” subhalos.

Table 3 shows the χ^2_ν values for each value of Δ . The fit is near $\chi^2_\nu \approx 1$ at all Δ , indicating that the fit is adequate to describing the data even though we have combined *all* the simulation outputs in the fit (i.e., all cosmologies and all redshifts).

3.3. Bias of High- ν Halos

The spherical collapse model is defined by a threshold for collapse that is independent of halo mass. However, peaks in the linear density field become increasingly elliptical and prolate at low ν , delaying collapse. Thus, in this mass regime, the barrier in the ellipsoidal collapse model is significantly higher than the constant δ_c assumed in spherical collapse calculations. As a result, collapsed low-mass halos reside in higher density environments, making them less abundant and more biased. At high ν , the ellipsoidal collapse barrier asymptotes to the spherical δ_c value and these two models should thus converge at high ν . However, the numerically-calibrated barrier used in the SMT fit asymptotes to a value lower than the spherical collapse δ_c in order to produce the abundance of high-mass halos (see the discussion in Robertson et al. 2009). Consequently, the clustering of high- ν halos in the SMT model is lower than the spherical collapse prediction.

In Figure 3a, we compare our fitting function to the formulae of the SMT and SC models for halos with $\nu > 1.5$. We also show the bias results from L500 and L1000W for four different redshifts and from L1280 for two redshifts. We focus on these simulations because they are the largest in our suite¹⁴. These are the same data presented in Figure 1, but here we are focusing on the high- ν regime. At $\nu \sim 2$, our simulation results are in good agreement with the SMT function, but at higher ν , our results rise above the SMT function and meet the spherical collapse prediction at $\nu \gtrsim 4$.

At high redshift ($z \sim 10$), Cohn & White (2008) found that the bias of $\nu \sim 3$ halos was better described by the SC models rather than SMT. However, two other recent studies of halo bias have concluded in favor of the SMT model for high-peak halos. In contrast to Cohn & White (2008), Reed et al. (2008) argue that the clustering of high- ν halos at $10 < z < 30$ in their simulations is better described by the SMT model. They claim that the bias measurements of Cohn & White (2008) are in error because the bias is calculated at $r = 1.5 h^{-1}$ Mpc, where the bias is scale-dependent. To correct for this, Reed et al. (2008) use a fitting function to extrapolate the translinear correlation function out to linear scales. Using this technique they find that SMT bias is a better fit than spherical collapse. Reed et al. (2008) are not able to calculate error bars for their bias values, and the matter variance over the total volume probed in their simulations is $\sim 12\%$ at the redshifts for which they obtain their results¹⁵, thus sample variance is still a concern. The numerical results of Pillepich et al. (2008) are also consistent with SMT at $2 \lesssim \nu \lesssim 3$, and deviate somewhat at higher masses. They use friends-of-friends (FOF) halos with a linking length of 0.2 times the mean interparticle separation, and they calculate halo bias by the ratio of the halo-matter power spectrum, $P_{hm}(k)$, to the matter power spectrum. Gao et al. (2005) and Angulo et al. (2008) use the halo-halo correlation

¹⁴ We do not include the 768 h^{-1} Mpc HOT simulation in this section because the results at high ν are possibly biased due to numerical issues. See the discussion in Appendix A of T08. We do include H768 in all fitting, but both the mass function and bias relation deviate from the mean results at high masses.

¹⁵ The matter variance of a $1 h^{-1}$ Mpc cube at $z = 10$ is 39%, but this is reduced by $\sqrt{11}$ due to the 11 realizations they have of this box.

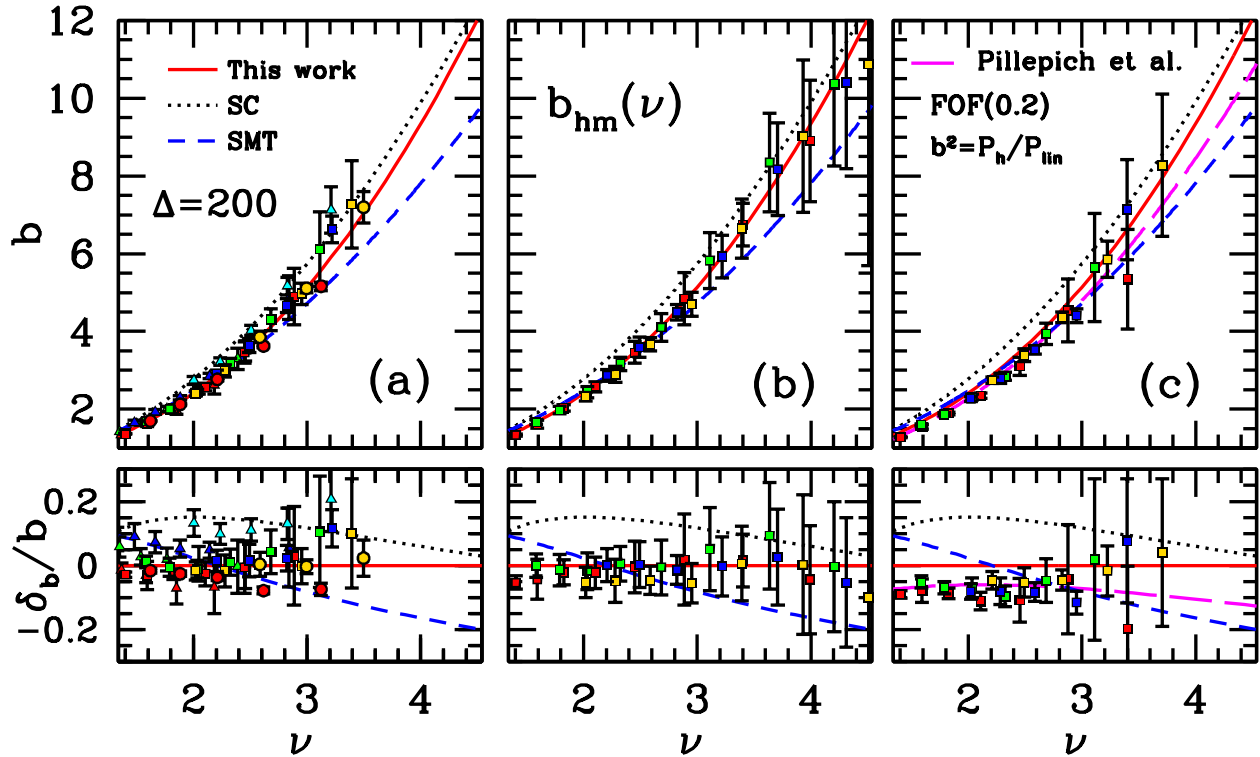


FIG. 3.— Panel (a): The $\Delta = 200$ bias function in the high- ν regime. The points with error bars represent our large-volume simulations at the redshifts listed in Table 1. Only points with fractional errors less than 25% are shown. The different colors, from left to right, go in order of increasing redshift: (red, green, yellow, blue, cyan)=(0.0, 0.5, 1.0, 1.25, 2.5). Like colors between simulations imply the same redshift. The dotted line is the spherical collapse prediction. The dashed line is the SMT function. The lower panel shows the fractional difference with respect to equation (6), $\delta_b = b_{\text{Nbody}} - b_{\text{fit}}$. Panel (b): Same as (a), but now using bias defined by the ratio of the $P_{hm}/P_{lin}(k)$. Results are shown for the L1000W simulation. Colors represent the same redshifts as in panel a. Panel (c): Bias of halos identified using the FOF algorithm with linking length 0.2. Bias is calculated from equation (2). Results are shown for the L1000W simulation. Different colors match to different redshifts as before. The dotted curve in this Figure is the fitting function of Pillepich et al. (2008), which is calibrated on FOF(0.2) halos.

TABLE 4
PARAMETER OF THE HALO MASS FUNCTION, EQUATION (8)

Δ	α	β	γ	ϕ	η
200	0.368	0.589	0.864	-0.729	-0.243
300	0.363	0.585	0.922	-0.789	-0.261
400	0.385	0.544	0.987	-0.910	-0.261
600	0.389	0.543	1.09	-1.05	-0.273
800	0.393	0.564	1.20	-1.20	-0.278
1200	0.365	0.623	1.34	-1.26	-0.301
1600	0.379	0.637	1.50	-1.45	-0.301
2400	0.355	0.673	1.68	-1.50	-0.319
3200	0.327	0.702	1.81	-1.49	-0.336

function to determine the bias of FOF(0.2) halos, with results similar to Pillepich et al. (2008).

In Figure 3a, our simulations prefer a model that is intermediate between SC and SMT. But in Figure 3b we explore the possible systematics involved in our estimate of $b(\nu)$. Here we use $P_{hm}(k)$ to determine $b(\nu)$ from L1000W. Because shot noise is no longer a concern, this statistic allows us to extend our bias measurements to higher masses at a given redshift output. Although the errors at high ν are large, the $z = 0$ results track our fit at all ν , demonstrating that these results

are not due to redshift evolution (and a lack of $z = 0$ data at $\nu > 2$). The results from other redshifts are also in agreement with the fit and with the $z = 0$ results using $P_{hm}(k)$.

The last systematic to be tested is the choice of halo-finding algorithm. In Figure 3c, we plot the bias of halos in the L1000W simulation that have been identified with the FOF(0.2) finder. The halos were defined using the same algorithm and linking length used by both Reed et al. (2008) and Pillepich et al. (2008). Although the difference with $\Delta = 200$ is small, there is a definite offset between the FOF(0.2) re-

sults and our $\Delta = 200$ fit. At $\nu \sim 3$, the SMT function is a reasonable description of the data. At higher ν the numerical results increase faster than the ν^2 scaling of SMT, but the errors are too large to see a significant difference with SMT. The empirical fit determined by Pillepich et al. (2008) is also a good fit to our FOF(0.2) data. Their fit is consistent with SMT at $\nu \sim 2-3$ and tends higher at larger ν . As discussed in T08 and Lukić et al. (2009), a significant fraction of FOF halos are actually two distinct density peaks linked together by the FOF algorithm. This linking increases the abundance of massive FOF halos relative to the abundance of SO halos and reduces the bias. The halo bias of the FOF(0.168) halo catalogs of Manera et al. (2009) agree with the $\Delta = 200$ results for the L1280 results.

3.4. NFW Scaling Between Values of Δ

One method of obtaining halo statistics at various values of Δ is to assume that halos are described by the density profile of Navarro et al. (1996) (hereafter NFW) and calculate the change in mass between the desired Δ and some fiducial value at which the mass function or bias relation is calibrated (i.e., Hu & Kravtsov 2003). In T08 we showed that this procedure leads to significant errors in the inferred mass function at $M < M_*$, and the abundance of high mass objects is sensitive to the model for halo concentrations used. In Figure 4 we test this procedure on the bias function. The curves represent the ratio between the bias obtained using the fitting functions of Table 2 the bias obtained by taking the $\Delta = 200$ bias function and rescaling it to higher overdensities. We assume the concentration-mass relation of Zhao et al. (2009) for all calculations, noting that the results on the high-mass end depend on the model used. Models that predict a lower concentration for cluster-sized halos, such as Bullock et al. (2001), yield a much stronger deviation from the N-body results. Scaling the masses from one Δ to another Δ can only result in a horizontal shift of the bias-mass relation; halos that were substructure at low Δ and revealed at high Δ are not taken into account. Low-mass substructures in high-mass halos that are “revealed” as host halos when Δ increases will increase the mean bias of these objects. This is why the rescaled bias function underpredicts halo bias at low ν .

At the high mass end, two effects alter the agreement between the measured bias and the rescaled bias. For the same object, the difference in halo mass between two values of Δ depends on the density profile of the halo. Thus, at a given M_{200} , scatter in the concentration-mass relation creates a distribution of halo masses at higher or lower Δ . Due to the steepness of the mass function at $\nu \gtrsim 1$, more low bias halos are scattered up to higher ν than high bias halos are scattered down. The calculation in Figure 4 assumes only the mean $c(M)$ relation. Scatter accounts for half of the discrepancy. The rest can be accounted for by the assembly bias of halos; the effect that halo properties correlate with large-scale environment (see, e.g., Sheth & Tormen 2004; Gao et al. 2005; Gao & White 2006; Wechsler et al. 2006). At $\nu \gtrsim 1$, more concentrated halos are less clustered than on average of the same mass. Thus, when scaling halos of the same M_{200} to higher M_Δ , the value of M_Δ depends on c and thus depends on bias such that higher values of M_Δ are less clustered. Using the result from Wechsler et al. (2006) that a $1\text{-}\sigma$ deviation in $\log c$ yields a $\sim 13\%$ deviation from the mean clustering for massive halos, scatter and assembly bias combined bring the rescaled bias function into agreement with the fitting functions at $\nu \gtrsim 1$.

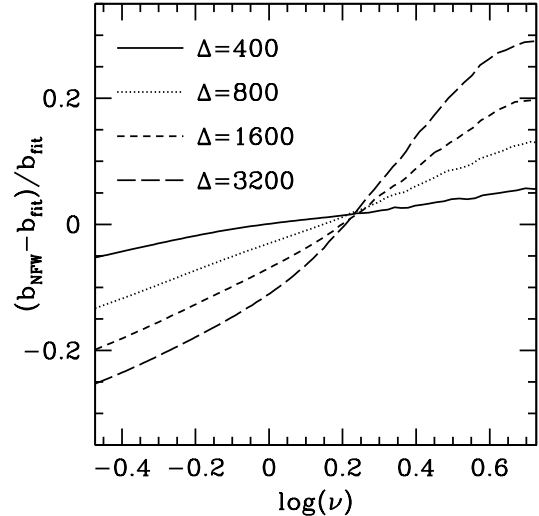


FIG. 4.— The fractional difference between the bias from fitting functions and the bias obtained from rescaling the $\Delta = 200$ fitting function to higher overdensities assuming NFW profiles and the concentration-mass relation of Zhao et al. (2009).

4. TESTING THE PEAK-BACKGROUND SPLIT

The mass function in Appendix C of T08 is written as a function of σ . To match with our parameterization of the bias function in equation (6) and to facilitate the peak-background split, we rewrite this function in terms of peak height ν . The original T08 function, $g(\sigma)$, is related to the new function by $g(\sigma) = \nu f(\nu)$, where

$$f(\nu) = \alpha \left[1 + (\beta\nu)^{-2\phi} \right] \nu^{2\eta} e^{-\gamma\nu^2/2}. \quad (8)$$

Table 4 lists the values of the five parameters of equation (8) for each value of delta.

The mass function parameters in Table 4 are set to match the $z = 0$ numerical results from T08. To model the redshift evolution of the $\Delta = 200$ mass function, the parameters have the following redshift dependence:

$$\beta = \beta_0 (1+z)^{0.20}, \quad (9)$$

$$\phi = \phi_0 (1+z)^{-0.08}, \quad (10)$$

$$\eta = \eta_0 (1+z)^{0.27}, \quad (11)$$

$$\gamma = \gamma_0 (1+z)^{-0.01}, \quad (12)$$

where β_0 , etc., is the value of the parameter at $z = 0$ as listed in Table 4. The value of α is obtained through the integral constraint in equation (7). The redshift-dependent fitting function is accurate to $\sim 5\%$ at $\nu > 0.6$ relative to the original T08 function. As discussed in T08, the rate of change of the mass function decreases as z increases, thus we recommend using the $z = 3$ in the above equations to obtain the mass function at $z > 3$.

Theoretical models for the halo mass function assume a one-to-one correspondence between peaks in the initial density field and collapsed objects that form at later times. The peak-background split obtains the bias of halo through the

change in the mass function (the distribution of density peaks) with the large-scale density field (the background). We implement the peak-background split under the common assumptions of the excursion set formalism, such as that the smoothing mass scale (for calculating $\sigma(M)$ in equation [3]) is the same as the mass in the collapsed halo (see Zentner 2007 for a review).

Following ST, we define the peak height, ν_1 , relative to the background, ν_0 , as

$$\nu_{10}^2 \equiv \frac{[\delta_1 - \delta_0]^2}{\sigma_1^2 - \sigma_0^2} \approx \nu_1^2 \left(1 - 2\frac{\delta_0}{\delta_1}\right), \quad (13)$$

where on the right hand side we have only kept the leading order terms. We Taylor expand $\nu_{10}f(\nu_{10})/\nu_1f(\nu_1)$ to calculate the Lagrangian halo peak-background split $\delta_h^L(\nu_1|\delta_0)$. Using equation 8, the overabundance of halos relative to the mean in Lagrangian space is

$$\delta_h^L(\nu_1|\delta_0) \approx \left[\gamma\nu_1^2 - (1+2\eta) + \frac{2\phi}{1+(\beta\nu_1)^2\phi} \right] \frac{\delta_0}{\delta_1} \equiv b_L(\nu_1)\delta_0. \quad (14)$$

This function is similar to Equation 11 of Sheth & Tormen (1999). The Eulerian bias is related to the Lagrangian bias by $b_E \equiv 1 + b_L$. If we set $\delta_1 = \delta_c$, the Eulerian bias is then

$$b(\nu) \approx 1 + \frac{\gamma\nu^2 - (1+2\eta)}{\delta_c} + \frac{2\phi/\delta_c}{1+(\beta\nu)^2\phi}. \quad (15)$$

Figure 5 compares peak-background split bias formula, equation (15), to our N-body calibrated results using equation (6). The peak-background split calculation does a reasonable job modeling the relative change in bias with Δ ; as the normalization of the mass function is lowered by increasing Δ , the amplitude of the bias function over the mass range probed increases. However, at all overdensities, the peak-background split overestimates the bias of low-mass halos. For low overdensities, $\Delta \leq 600$, equation (15) overestimates the bias of halos above the non-linear mass threshold. For higher overdensities, the N-body and analytic results appear consistent for high-peak halos, although the two curves must diverge eventually, as $b \sim \nu^2$ in the peak-background split and $b \sim \nu^{2.4}$ in our numerical fit. By definition, equation (15) satisfies the integral constraint in equation (7), as does the numerical fit; at $\log \nu < -0.5$, the bias from equation (6) is higher than the peak-background split calculation.

At high masses at low overdensities, our results are consistent with those found in Manera et al. (2009). Using FOF-based halos, they find that employing the peak-background split on the mass function derived directly from their halo catalogs underpredicts the bias of high-peak halos. They find this result for three different values of the FOF linking parameter, 0.2, 0.168, and 0.15. As the linking length is reduced—which is analogous to increasing the halo overdensity Δ —the discrepancy is reduced but never completely goes away. From T08, the linking length best associated with $\Delta = 1600$ is 0.1, significantly lower than the three values used by Manera et al. (2009). Given the trends in their results and in Figure 5, we predict that the peak-background split will yield consistent results at $l \lesssim 0.12$, but only at the high-mass end of the spectrum.

5. SUMMARY AND DISCUSSION

We have presented a series of calibrated fitting functions for large-scale halo bias. The fitting functions are designed to yield the bias factor for any value of Δ within the calibrated range. These functions are normalized such that, when used in concert with the normalized mass functions of T08 (given by equations [8]-[12] in this paper), the overall bias of dark matter is unity. We find a $\sim 6\%$ scatter from simulation-to-simulation. Combined with the 5% error in the T08 mass function, this level of uncertainty has a non-negligible impact on the precision with which cosmological parameters can be constrained from cluster abundance studies; the Dark Energy Figure-of-Merit (Albrecht et al. 2006) is reduced by 25-50%, depending on the details of the survey (Cunha & Evrard 2009; Wu et al. 2009). More importantly, T08 and this study focus exclusively on cosmological parameters in which the vacuum energy density is constant with redshift. More study is required to determine if the halo bias function is universal with variations in universal expansion and growth history induced by dark energy. For cluster studies, where the primary concern is the abundance of massive objects, a series of large-volume simulations similar to L1000W are required to address this uncertainty. To isolate the effects of dark energy in both the mass function and bias function, using the same initial phases with different dark energy equations of state would eliminate sample variance, which is a concern even for h^{-1} Gpc simulations.

Within the precision of our data set, the numerical results do not show evidence for significant evolution of bias with redshift. Any evolution must be at the $\lesssim 5\%$ level over our redshift baseline. This finding contrasts with our results from the mass function; in T08 we demonstrated that the SO mass function evolves by up to $\sim 50\%$ from $z = 0$ to $z = 2.5$. This evolution is more pronounced with higher overdensity. If the abundance of dark matter halos is connected to the bias of halos—as is assumed in the peak-background split—one would assume that b should increase at fixed ν as redshift increases. To the statistical precision of our data, however, halo bias can be modeled by a single, redshift-independent function.

Although the absolute predictions of the peak-background split fail to reproduce our numerical results in detail, this method reasonably tracks the change in the bias function with Δ . Thus we can gain insight from using the peak-background split on the mass function at various redshifts to see how it changes under the peak-background ansatz. In T08, the evolution in the mass function is mostly encompassed by a change in the overall normalization of $\nu f(\nu)$ (cf., Figure 6 in T08), with a slightly stronger evolution for $\nu \gtrsim 1$ halos. A change in the overall abundance of halos does not induce a change in their clustering. Thus, employing the peak-background split on the redshift-dependent mass function for $\Delta = 200$ at $z = 1.25$ yields a bias function that is at nearly identical to the $z = 0$ peak-background split function at high ν , and is only $\sim 5\%$ higher at $\nu \lesssim 0.4$.

We have paid significant attention to the bias of halos at $\nu \gtrsim 2$, which corresponds to the peak-height for galaxy clusters. Our $\Delta = 200$ halo catalogs disfavor a bias function with an amplitude as low as SMT. This result is robust to any choice of statistic with which to calculate the bias. The numerical results of Reed et al. (2008) and Pillepich et al. (2008) find good agreement with SMT at these scales, but these results are based on FOF(0.2) halos. The known problem of linking distinct objects in the FOF algorithm would reduce bias at fixed mass because two (or more) objects with intrinsically

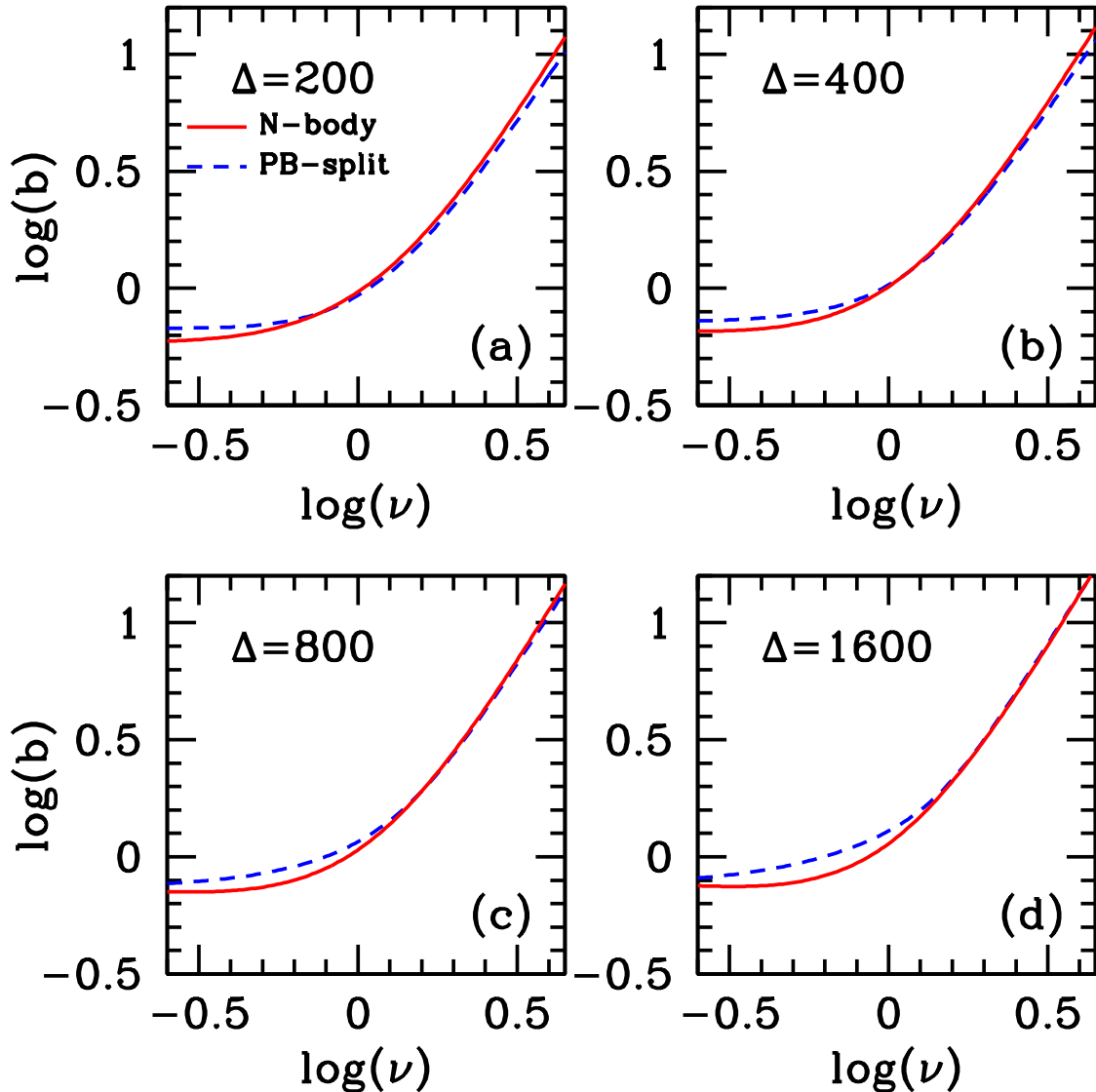


FIG. 5.— Comparison of halo bias calibrated from our numerical simulations, equation (6), with results from the peak-background split, equation (15). At $\Delta = 200$, the peak-background split calculation is $\sim 20\%$ high/low and low/high ν . As Δ increases, the residuals at $\nu > 1$ become smaller while the residuals at $\nu < 1$ become larger.

lower bias are being counted as one more massive object. In addition, as pointed out in Lukić et al. (2009), the mean ratio between FOF halo mass and SO halo mass depends on concentration even for unbridged samples of halos, so this will also affect the relative bias between the two mass definitions in a non-trivial manner. In our simulations, $\Delta = 200$ and FOF(0.2) do not agree. At $\nu = 3$, our FOF(0.2) results appear to be in agreement with the SMT function as well as the fitting function of Pillepich et al. (2008).

In a general sense, the peak-background split does achieve marked success; the first-order derivation calculated here is accurate to $\lesssim 20\%$ and correctly predicts the change in bias with Δ . There are several possibilities in explaining the differences between the theory and N-body results. For massive halos, a first-order expansion of the peak-background split may not be sufficient. However, Manera et al. (2009) and Manera & Gaztanaga (2009) demonstrate that higher-order terms do increase the accuracy of the calculation at high

masses, but decreases it at lower masses. The growth of low-mass halos in overdensities is truncated due to the presence of nearby, high-mass objects (Wechsler et al. 2006; Wang et al. 2007; Dalal et al. 2008; Hahn et al. 2009). Our implementation of the peak-background split assumes that the local peak corresponding to the collapse threshold is $\delta_1 = \delta_c = 1.686$, ignoring any environmental effects on the collapse of dark matter halos. Alternatively, as discussed in Manera et al. (2009), it is not clear that the mass that enters into the calculation of the peak height, $\delta_c/\sigma(M)$, should be the same mass of the object that eventually collapses. The mass contained within the peak does not completely map onto the mass within the collapsed halo (Dalal et al. 2008). It remains to be seen whether a more robust implementation of the peak-background split model, in which the Taylor expansion is replaced with a more rigorous treatment, can reconcile the differences between theory and numerical results, or if the peak-background split fails at a more fundamental level. More work is required to isolate

the failures of the model and bring our theoretical understanding of the formation of dark matter halos into agreement with the ever-increasing precision of numerical simulations.

We thank Roman Scoccimarro for sharing his N-body simulations and for the computational resources to analyze them. BER is supported by a Hubble Fellowship grant, program number HST-HF-51262.01-A provided by NASA from the Space Telescope Science Institute, which is operated by the Association of Universities for Research in Astronomy, Incorporated, under NASA contract NAS5-26555. AVK is supported by the NSF under grants No. AST-0239759 and AST-0507666, by NASA through grant NAG5-13274, and by the Kavli Institute for Cosmological Physics at the University of

Chicago. Portions of this work were performed under the auspices of the U.S. Dept. of Energy, and supported by its contract #W-7405-ENG-36 to Los Alamos National Laboratory. Computational resources were provided by the LANL open supercomputing initiative. SG acknowledges support by the German Academic Exchange Service. Some of the simulations were performed at the Leibniz Rechenzentrum Munich, partly using German Grid infrastructure provided by AstroGrid-D. The GADGET SPH simulations have been done in the MareNostrum supercomputer at BSC-CNS (Spain) and analyzed at NIC Jülich (Germany). G.Y. and S.G. wish to thank A.I. Hispano-Alemanas and DFG for financial support. G.Y. acknowledges support also from M.E.C. grants FPA2006-01105 and AYA2006-15492-C03.

REFERENCES

- Abazajian, K., Zheng, Z., Zehavi, I., Weinberg, D. H., Frieman, J. A., Berlind, A. A., Blanton, M. R., Bahcall, N. A., Brinkmann, J., Schneider, D. P., & Tegmark, M. 2005, *ApJ*, 625, 613
- Albrecht, A., Bernstein, G., Cahn, R., Freedman, W. L., Hewitt, J., Hu, W., Huth, J., Kamionkowski, M., Kolb, E. W., Knox, L., Mather, J. C., Staggs, S., & Suntzeff, N. B. 2006, *arXiv:astro-ph/0609591*
- Angulo, R. E., Baugh, C. M., & Lacey, C. G. 2008, *MNRAS*, 387, 921
- Arnaud, M., Pointecouteau, E., & Pratt, G. W. 2007, *A&A*, 474, L37
- Arnaud, M., Pratt, G. W., Piffaretti, R., Boehringer, H., Croston, J. H., & Pointecouteau, E. 2009, *ã*, (submitted), *ArXiv:0910.1234*
- Bardeen, J. M., Bond, J. R., Kaiser, N., & Szalay, A. S. 1986, *ApJ*, 304, 15
- Bialek, J. J., Evrard, A. E., & Mohr, J. J. 2001, *ApJ*, 555, 597
- Bullock, J. S., Kolatt, T. S., Sigad, Y., Somerville, R. S., Kravtsov, A. V., Klypin, A. A., Primack, J. R., & Dekel, A. 2001, *MNRAS*, 321, 559
- Cohn, J. D. & White, M. 2008, *MNRAS*, 385, 2025
- Cole, S. & Kaiser, N. 1989, *MNRAS*, 237, 1127
- Croce, M., Puelbas, S., & Scoccimarro, R. 2006, *MNRAS*, 373, 369
- Cunha, C. E. & Evrard, A. E. 2009, *Phys. Rev. D*, submitted, *ArXiv:0908.0526*
- da Silva, A. C., Kay, S. T., Liddle, A. R., & Thomas, P. A. 2004, *MNRAS*, 348, 1401
- Dalal, N., White, M., Bond, J. R., & Shirokov, A. 2008, *ApJ*, 687, 12
- Davis, M., Efstathiou, G., Frenk, C. S., & White, S. D. M. 1985, *ApJ*, 292, 371
- Dunkley, J., Komatsu, E., Nolta, M. R., Spergel, D. N., Larson, D., Hinshaw, G., Page, L., Bennett, C. L., Gold, B., Jarosik, N., Weiland, J. L., Halpern, M., Hill, R. S., Kogut, A., Limon, M., Meyer, S. S., Tucker, G. S., Wollack, E., & Wright, E. L. 2009, *ApJS*, 180, 306
- Eke, V. R., Cole, S., Frenk, C. S., & Patrick Henry, J. 1998, *MNRAS*, 298, 1145
- Gao, L., Springel, V., & White, S. D. M. 2005, *MNRAS*, 363, L66
- Gao, L. & White, S. D. M. 2006
- Gottlöber, S. & Klypin, A. 2008, *ArXiv:0803.4343*
- Gross, M. A. K., Somerville, R. S., Primack, J. R., Holtzman, J., & Klypin, A. 1998, *MNRAS*, 301, 81
- Hahn, O., Porciani, C., Dekel, A., & Carollo, C. M. 2009, *MNRAS*, 398, 1742
- Hu, W. & Kravtsov, A. V. 2003, *ApJ*, 584, 702
- Jenkins, A., Frenk, C. S., White, S. D. M., Colberg, J. M., Cole, S., Evrard, A. E., Couchman, H. M. P., & Yoshida, N. 2001, *MNRAS*, 321, 372
- Jing, Y. P. 1998, *ApJ*, 503, L9+
- 1999, *ApJ*, 515, L45
- 2005, *ApJ*, 620, 559
- Kaiser, N. 1984, *ApJ*, 284, L9
- Kravtsov, A. V., Klypin, A. A., & Khokhlov, A. M. 1997, *ApJS*, 111, 73
- Kravtsov, A. V., Vikhlinin, A., & Nagai, D. 2006, *ApJ*, 650, 128
- Lacey, C. & Cole, S. 1994, *MNRAS*, 271, 676
- Lee, J. & Shandarin, S. F. 1999, *ApJ*, 517, L5
- Lima, M. & Hu, W. 2004, *Phys. Rev. D*, 70, 043504
- 2005, *Phys. Rev. D*, 72, 043006
- Lukić, Z., Reed, D., Habib, S., & Heitmann, K. 2009, *ApJ*, 692, 217
- Majumdar, S. & Mohr, J. J. 2004, *ApJ*, 613, 41
- Mandelbaum, R., Tasitsiomi, A., Seljak, U., Kravtsov, A. V., & Wechsler, R. H. 2005, *MNRAS*, 362, 1451
- Manera, M. & Gaztanaga, E. 2009, *MNRAS*, submitted, *ArXiv:0912.0446*
- Manera, M., Sheth, R. K., & Scoccimarro, R. 2009, *MNRAS* (in press), *arXiv:0906.1314*, 1826
- Mo, H. J. & White, S. D. M. 1996, *MNRAS*, 282, 347
- Mohr, J. J., Mathiesen, B., & Evrard, A. E. 1999, *ApJ*, 517, 627
- Nagai, D. 2006, *ApJ*, 650, 538
- Navarro, J. F., Frenk, C. S., & White, S. D. M. 1996, *ApJ*, 462, 563
- Oguri, M. 2009, *Physical Review Letters*, 102, 211301
- Pillepich, A., Porciani, C., & Hahn, O. 2008, *ArXiv:0811.4176*
- Press, W. H. & Schechter, P. 1974, *ApJ*, 187, 425
- Reed, D. S., Bower, R., Frenk, C. S., Jenkins, A., & Theuns, T. 2008, *ArXiv e-prints*, *arXiv:0804.0004* [astro-ph]
- Robertson, B. E., Kravtsov, A. V., Tinker, J., & Zentner, A. R. 2009, *ApJ*, 696, 636
- Seljak, U. & Warren, M. S. 2004, *MNRAS*, 355, 129
- Sheth, R. K., Mo, H. J., & Tormen, G. 2001, *MNRAS*, 323, 1
- Sheth, R. K. & Tormen, G. 1999, *MNRAS*, 308, 119
- 2004, *MNRAS*, 350, 1385
- Spergel, D. N., Verde, L., Peiris, H. V., Komatsu, E., Nolta, M. R., Bennett, C. L., Halpern, M., Hinshaw, G., Jarosik, N., Kogut, A., Limon, M., Meyer, S. S., Page, L., Tucker, G. S., Weiland, J. L., Wollack, E., & Wright, E. L. 2003, *ApJS*, 148, 175
- Springel, V. 2005, *MNRAS*, 364, 1105
- Sun, M., Voit, G. M., Donahue, M., Jones, C., Forman, W., & Vikhlinin, A. 2009, *ApJ*, 693, 1142
- Tinker, J., Kravtsov, A. V., Klypin, A., Abazajian, K., Warren, M., Yepes, G., Gottlöber, S., & Holz, D. E. 2008, *ApJ*, 688, 709
- Tinker, J. L., Weinberg, D. H., Zheng, Z., & Zehavi, I. 2005, *ApJ*, 631, 41
- van den Bosch, F. C., Mo, H. J., & Yang, X. 2003, *MNRAS*, 345, 923
- Vikhlinin, A., Kravtsov, A., Forman, W., Jones, C., Markevitch, M., Murray, S. S., & Van Speybroeck, L. 2006, *ApJ*, 640, 691
- Vikhlinin, A., Kravtsov, A. V., Burenin, R. A., Ebeling, H., Forman, W. R., Hornstrup, A., Jones, C., Murray, S. S., Nagai, D., Quintana, H., & Voevodkin, A. 2009, *ApJ*, 692, 1060
- Wang, H. Y., Mo, H. J., & Jing, Y. P. 2007, *MNRAS*, 375, 633
- Warren, M. S., Abazajian, K., Holz, D. E., & Teodoro, L. 2006, *ApJ*, 646, 881
- Wechsler, R. H., Zentner, A. R., Bullock, J. S., Kravtsov, A. V., & Allgood, B. 2006, *ApJ*, 652, 71
- White, M. 2001, *A&A*, 367, 27
- Wu, H., Zentner, A. R., & Wechsler, R. H. 2009, *ApJ*, (submitted), *ArXiv:0910.3668*
- Yoo, J., Weinberg, D. H., Tinker, J. L., Zheng, Z., & Warren, M. S. 2009, *ApJ*, 698, 967
- Zehavi, I., Zheng, Z., Weinberg, D. H., Frieman, J. A., Berlind, A. A., Blanton, M. R., Scoccimarro, R., Sheth, R. K., Strauss, M. A., Kayo, I., Suto, Y., Fukugita, M., Nakamura, O., Bahcall, N. A., Brinkmann, J., Gunn, J. E., Hennessee, G. S., Ivezić, Ž., Knapp, G. R., Loveday, J., Meiksin, A., Schlegel, D. J., Schneider, D. P., Szapudi, I., Tegmark, M., Vogeley, M. S., & York, D. G. 2005, *ApJ*, 630, 1
- Zentner, A. R. 2007, *International Journal of Modern Physics D*, 16, 763
- Zhang, Y.-Y., Finoguenov, A., Böhringer, H., Kneib, J.-P., Smith, G. P., Kneissl, R., Okabe, N., & Dahle, H. 2008, *A&A*, 482, 451
- Zhao, D. H., Jing, Y. P., Mo, H. J., & Börner, G. 2009, *ApJ*, 707, 354
- Zheng, Z. & Weinberg, D. H. 2007, *ApJ*, 659, 1